Enhanced Antibacterial and Anticancer Activities of Soy Protein Isolate through Conjugation with Iron Oxide and Zinc Oxide Nanoparticles

Ramy M. Romeilah,[a] Solafa Abdelhakim,[b] Mohamed Raafat Atteya,[c] Sayed E. Younis,[d] Khaled M. A. Ramadan,[e] Hossam S. El-Beltagi,[f]* Gamal Enan,[g] Ahmed Maher Gaber,[c] Mahmoud M. El-saber,[h] Nada Ali AboZaid,[i] and Ali Osman [j,]*

* *Corresponding authors: helbeltagi@kfu.edu.sa; aokhalil@zu.edu.eg*

DOI: 10.15376/biores.21.4.10127-10148

GRAPHICAL ABSTRACT

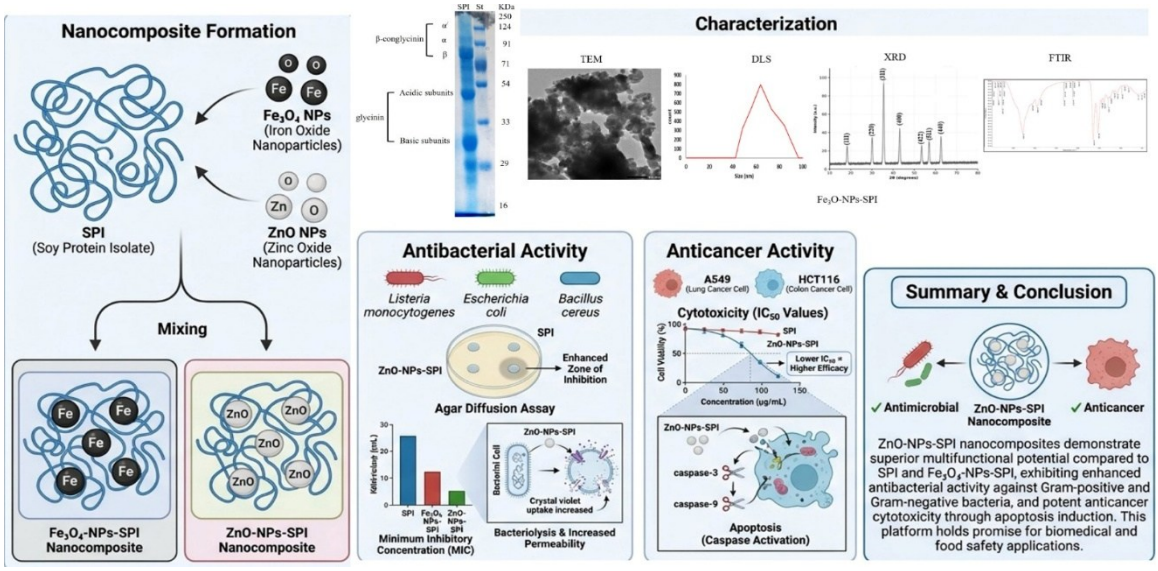

Enhanced Antibacterial and Anticancer Activities of Soy Protein Isolate through Conjugation with Iron Oxide and Zinc Oxide Nanoparticles

Ramy M. Romeilah,[a] Solafa Abdelhakim,[b] Mohamed Raafat Atteya,[c] Sayed E. Younis,[d] Khaled M. A. Ramadan,[e] Hossam S. El-Beltagi,[f,*] Gamal Enan,[g] Ahmed Maher Gaber,[c] Mahmoud M. El-saber,[h] Nada Ali AboZaid,[i] and Ali Osman [j,*]

Soy protein isolate (SPI) was utilized as a biocompatible matrix for the development of Fe_3O_4 and ZnO nanoparticle composites with enhanced biological activities. The synthesized nanocomposites were characterized using various analytical methods that confirmed the successful nanoparticle formation and conjugation with SPI. Antibacterial activity was evaluated against *L. monocytogenes*, *E. coli*, and *B. cereus* using agar well diffusion, minimum inhibitory concentration (MIC), growth kinetics, crystal violet uptake, and cell lysis assays. Both nanocomposites exhibited superior antibacterial efficacy compared with SPI alone, with ZnO-based composites demonstrating the strongest broad-spectrum activity. Nanoformulation reduced MIC values by up to eightfold and significantly enhanced membrane permeability and bacteriolytic effects. The anticancer potential of tested materials was assessed against A549 and HCT116 cell lines. ZnO-NPs-SPI showed the highest cytotoxicity, producing IC_{50} values of 27.8 and 31.25 µg/mL against A549 and HCT116 cells, respectively. Furthermore, treatment induced significant activation of caspase-3 and caspase-9, indicating apoptosis-mediated cell death. These findings demonstrate that SPI-based nanocomposites, particularly those containing ZnO-NPs, represent promising multifunctional platforms for antimicrobial and anticancer applications.

DOI: 10.15376/biores.21.4.10127-10148

Keywords: Green synthesis; Nanocomposites; Apoptosis; Caspase activation; Membrane disruption; Biocompatible carrier

*Contact information: a: Department of Chemistry, College of Science, University of Hail, Saudi Arabia; b: Department of Plant Production (Microbiology Specialization), Faculty of Development and Technology, Zagazig University, Zagazig, 44519, Egypt; c: Department of Physical Therapy, College of Applied Medical Sciences, University of Hail, Hail 81451, Saudi Arabia; d: Department of Plant Production (Plant Pathology Specialization), Faculty of Development and Technology, Zagazig University, Zagazig, 44519, Egypt; e: Central Laboratories, Department of Chemistry, King Faisal University, Al-Ahsa 31982, Saudi Arabia; f: Agricultural Biotechnology Department, College of Agriculture and Food Sciences, King Faisal University, Al-Ahsa 31982, Saudi Arabia; g: Department of Botany and Microbiology, Faculty of Science, Zagazig University, Zagazig, 44519, Egypt; h: Biochemistry Unit, Genetic Resources Department, Desert Research Center, El-Matarya, Cairo 11753, Egypt; i: Department of Health Management, College of Public Health and Health Informatics, University of Hail, Hail, Saudi Arabia; j: Department of Biochemistry, Faculty of Agriculture, Zagazig University, Zagazig, 44519, Egypt; * Corresponding authors: helbeltagi@kfu.edu.sa; aokhalil@zu.edu.eg*

INTRODUCTION

Soybean protein isolate (SPI) mainly consists of reserve proteins belonging to high-molecular weight globulin family (Chen *et al.* 2025). Soybean storage proteins are primarily classified into glycinin (11S) and β-conglycinin (7S). Glycinin (~360 kDa) is a hexameric protein composed of acidic and basic polypeptide subunits interconnected through disulfide linkages (Yang *et al.* 2025). β-Conglycinin differs from glycinin as it is a glycosylated trimer with a molecular weight ranging from 150 to 200 kDa (Wu *et al.* 2023). These storage proteins not only serve nutritional roles but also exhibit bioactive properties, making SPI a valuable candidate for functional food and biomedical applications (Sitohy and Osman 2010; Turmagambetova *et al.* 2015).

Microbial activity is essential in food systems, but it may also result in spoilage and pathogen contamination, thereby compromising food safety and increasing health risks (Sitohy *et al.* 2011; Osman *et al.* 2013). Common bacterial pathogens include *Bacillus cereus*, *Clostridium botulinum*, *Campylobacter* spp., *Clostridium perfringens*, certain *Escherichia coli* serogroups, *Listeria monocytogenes*, *Salmonella* spp., *Shigella* spp., *Staphylococcus aureus*, and *Vibrio* spp (Abdel-Hamid *et al.* 2020; Lianou *et al.* 2023). Development of antimicrobial agents from natural sources has become increasingly important due to their potential to mitigate threats associated with foodborne bacterial pathogens (Abdel-Hamid *et al.* 2016; Farid *et al.* 2023).

SPI was selected as the biopolymeric carrier matrix in the present study on the basis of several converging scientific rationales. First, its constituent proteins — glycinin (11S) and β-conglycinin (7S) — provide an abundance of reactive functional groups (–NH_2, –COOH, –SH, –OH) that facilitate stable coordination and conjugation with metal oxide nanoparticles including ZnO and Fe_3O_4 (Schmidt 2023; Lan *et al.* 2024). Second, the amphiphilic character of SPI supports the formation of small, monodisperse, and colloidally stable nanoparticle conjugates that remain stable across the pH and ionic conditions used in antibacterial and cytotoxicity assays (Pujara *et al.* 2017; Hui *et al.* 2024). Third, unlike animal-derived protein carriers such as casein, whey, or gelatin, SPI possesses documented intrinsic antibacterial bioactivity (Sitohy and Osman 2010; Turmagambetova *et al.* 2015), enabling synergistic rather than merely additive interactions with conjugated nanoparticles. Fourth, SPI is plant-derived, biodegradable, and biocompatible, with established application in biomedical carrier systems (Tansaz and Boccaccini 2016; Reddy and Rapisarda 2021). Animal-derived carriers including gelatin (collagen-derived, batch-variable, immunogenic) and casein (pH-sensitive micelle disassembly, dairy origin) were considered but deemed less suitable given the alkaline synthesis conditions required, the food-safety scope of the work, and the absence of documented ZnO/Fe_3O_4 conjugation precedent for those matrices. Together, these properties justify SPI as the preferred biopolymeric carrier for nanocomposite development in the present study.

Nanotechnology has significantly contributed to improving antimicrobial performance (Elshafie *et al.* 2023; El-Beltagi *et al.* 2024a). The design and synthesis of nanoscale materials with antimicrobial potential have attracted considerable scientific interest. Key applications include diagnostics, imaging, and smart drug delivery systems that enhance therapeutic efficiency through site-specific targeting (El-Beltagi *et al.* 2024b; El-Beltagi *et al.* 2025). Broad variety of nanomaterials has been designed to target harmful microorganisms, particularly bacteria (Mourad *et al.* 2025).

Assessing foodborne pathogens and their metabolites is important for risk evaluation and food safety management. Some toxic metabolites, particularly carcinogenic ones, can remain in food despite removal of microorganisms that produced them (Taiwo *et al.* 2024). Cancer is a major global health concern and remains among the primary causes of illness and death worldwide (Almutairi *et al.* 2025). It is characterized by abnormal and uncontrolled cell growth, tissue invasion, and ability to spread to distant sites through metastasis. Although current treatment modalities, such as surgery, chemotherapy, radiotherapy, immunotherapy, and targeted therapies, have enhanced survival rates, their clinical utility is often constrained by adverse effects, therapeutic resistance, high costs, and unintended toxicity to normal cells. These limitations have stimulated increasing interest in identifying novel anticancer compounds from natural resources as safer and more effective therapeutic alternatives (Abd El-Halim *et al.* 2026). Natural bioactive compounds exhibit promising anticancer properties because of their biocompatibility and low toxicity. Nanotechnology further enhances their stability, bioavailability, and targeting efficiency, improving therapeutic effectiveness and safety. Recent advances in nanotechnology have enabled conjugation of SPI with inorganic nanoparticles such as ZnO-NPs-SPI and Fe_3O_4-NPs-SPI (El-Saber *et al.* 2021). Such conjugates are hypothesized to enhance the intrinsic bioactivity of SPI by improving stability, bioavailability, and biological interactions. Nanoparticles based on zinc and iron oxides (ZnO-NPs and Fe_3O_4-NPs) are well-documented for their antimicrobial and cytotoxic effects, and their integration with SPI may yield synergistic outcomes. In this study, SPI and its nanoparticle conjugates (ZnO-NPs-SPI and Fe_3O_4-NPs-SPI) were evaluated for their antibacterial activity against *L. monocytogenes*, *E. coli*, and *B. cereus*, as well as their cytotoxicity against human lung carcinoma A549 and human lung carcinoma HCT116 cell lines.

EXPERIMENTAL

Soybean Protein Isolates (SPI) Preparation

Soybean seeds were obtained from a local market in Zagazig City, Sharkia, Egypt, cleaned, milled, and sieved (1.0 mm). The flour was defatted using a chloroform–methanol mixture (3:1, v/v), and the solvent was evaporated (Rotary evaporator, Buchi, Switzerland). Defatted flour was extracted in water at pH 9, followed by centrifugation at 2000 ×g for 15 min using a centrifuge (Jouan, France). Proteins were precipitated at pH 4.5, recovered by centrifugation at 2000 ×g for 15 min, washed, neutralized, dialyzed overnight, and freeze-dried to obtain SPI (Johnson and Brekke 1983).

SDS-PAGE

Sodium dodecyl sulfate–polyacrylamide gel electrophoresis (SDS–PAGE) of SPI was conducted using (Laemmli 1970) discontinuous buffer system. Separation gels (10%) and stacking gels (3%) were polymerized with tetramethyl-ethylenediamine (TEMED) and ammonium persulfate as critical catalyst-initiator pair. SPI samples (5 mg) were solubilized in Tris buffer, mixed with SDS sample buffer, heated at 96 °C, and electrophoresed. Gels were incubated with Coomassie Brilliant Blue R-250 for protein visualization and subsequently destained. Molecular masses of protein bands were determined by comparing their migration patterns with those of reference protein standards.

Green Synthesis of Fe_3O_4-NPs and ZnO-NPs using L-ascorbic Acid

The synthesis of Fe_3O_4-NPs and ZnO-NPs was carried out using L-ascorbic acid as both a reducing and capping agent (Tewatia *et al.* 2022; Enan *et al.* 2026). Aqueous solutions of 1.34 g $FeCl_2.4H_2O$ and 3.40 g $FeCl_3.6H_2O$ for Fe_3O_4-NPs, and 1 mM zinc nitrate hexahydrate [$Zn(NO_3)_2.6H_2O$] solution for ZnO-NPs were each dissolved separately in 60 mL of deionized water. The mixture was heated to 80 °C for magnetite and 85 °C for zinc under vigorous magnetic stirring until the solution became homogeneous and no visible solid residues were observed. Then, an aqueous solution of L-ascorbic acid (50 mM) was added dropwise to each precursor solution. The reaction mixtures were then adjusted to an alkaline pH (10) by the dropwise addition of 5 mL of 1% NaOH. The resulting mixtures were further stirred for 1h, during which a gradual color change to dark brown for Fe_3O_4-NPs and white color for ZnO-NPs occurred. Finally, the deionized water was added to the reaction mixtures to reach a final concentration of 1000 µg/mL. After overnight incubation at room temperature, the mixtures were subjected to ultrasonic treatment (sonication) for 30 min at a temperature of 35 °C to enhance nanoparticle dispersion and prevent agglomeration. The resulting Fe_3O_4-NPs and ZnO-NPs were collected by centrifugation, washed repeatedly with distilled water, and the pellets of ZnO-NPs were dried and calcinated for 2 h at 300 °C.

Conjugation of Fe_3O_4-NPs and ZnO-NPs with SPI

One hundred milligrams of SPI was dissolved in 25 mL of Milli-Q water and 25 mL of Fe_3O_4-NPs and ZnO-NPs solution were added (1000 µg/mL stock solution), and vigorously vortexed for 10 min, followed by sonication for 30 min.

Nanoparticle Content and SPI Loading Composition

The conjugation reaction combined 100 mg SPI with 25 mg Fe_3O_4-NPs or ZnO-NPs (25 mL of a 1000 µg/mL stock) in a total volume of 50 mL, corresponding to a nominal nanoparticle loading of 20% w/w (nanoparticle-to-SPI mass ratio of 1:4) at an overall solids concentration of 2.5 mg/mL.

Characterization of Nanoparticles

TEM

Morphology and size of Fe_3O_4-NPs, ZnO-NPs, Fe_3O_4-NPs-SPI, and ZnO-NPs-SPI were characterized by transmission electron microscopy (TEM) operated at 100 kV connected with a CCD camera, Japan.

DLS

Dynamic light scattering (DLS) was employed to determine hydrodynamic diameter, size distribution profile of Fe_3O_4-NPs, ZnO-NPs, Fe_3O_4-NPs-SPI, and ZnO-NPs-SPI suspended in solution.

XRD

X-ray diffraction (XRD) analysis was performed using a Bruker D8 Discover diffractometer (Billerica, MA, USA) to evaluate the crystalline characteristics of Fe_3O_4 and ZnO nanoparticles and to verify their successful synthesis, phase purity, and structural uniformity.

FTIR

Surface functional groups of synthesized nanoparticles were identified using FTIR spectroscopy (Thermo Nicolet 6700). Spectra were obtained by the KBr pellet technique over the 400 to 4000 cm^{-1} range at a spectral resolution of 4 cm^{-1}.

Antibacterial Activity Evaluation

Microorganisms

The foodborne pathogenic bacterial strains of *L. monocytogenes, E. coli*, and *B. cereus* were obtained from Botany and Microbiology Department, Faculty of Science, Zagazig University, Zagazig, Egypt.

Agar-well diffusion assay

Antibacterial activities of SPI, Fe_3O_4-NPs-SPI, and ZnO-NPs-SPI were evaluated using agar well diffusion method (Nanda *et al.* 2009). Pure cultures of *L. monocytogenes*, *E. coli*, and *B. cereus* were grown in brain heart infusion broth (BHIB) at 37 °C with shaking (200 rpm) until the exponential phase, then adjusted to ~1.0×10^9 CFU/mL. Each strain was spread uniformly on BHI agar plates using sterile swabs, and wells (6 mm diameter) were prepared with a sterile gel puncher. Aliquots (40 µL) of SPI, Fe_3O_4-NPs-SPI, and ZnO-NPs-SPI solutions at concentrations of 31.25, 62.5, 125, 250, 500, and 1000 µg/mL were added to the wells. Plates were incubated at 37 °C for 24 h, and inhibition zones were measured in millimeters using a transparent ruler.

Minimum inhibitory concentration

Minimum inhibitory concentration (MIC) of SPI, Fe_3O_4-NPs-SPI, and ZnO-NPs-SPI was determined using the broth microdilution technique. Exponential-phase cultures of *L. monocytogenes*, *E. coli*, and *B. cereus* were adjusted to ~1×10^6 CFU/mL in BHIB. Serial two-fold dilutions of each treatment (3.9 to 1000 µg/mL) were prepared in 96-well microplates, inoculated with bacterial suspensions, and incubated at 37 °C for 24 h. The MIC values were recorded as lowest concentration showing no visible growth compared to untreated controls (Wiegand *et al.* 2008).

Bacterial growth curve

Bacterial growth curves were determined by turbidity assay. Aliquots (50 µL) of *L. monocytogenes*, *E. coli*, and *B. cereus* cultures (grown for 4 h in BHIB at 37 °C) were dispensed into 96-well microplates. Cells were treated with 50 µL of SPI, Fe_3O_4-NPs-SPI, and ZnO-NPs-SPI at the respective MIC of each treatment for the corresponding bacterial strain. Negative controls contained only broth, while positive controls contained untreated cultures. Growth was monitored by optical density at 600 nm using a microplate reader (Bio-Rad 680XR, Hertfordshire, U.K.) at 0, 6, 12, 18, and 24 h (Sitohy and Osman 2010).

Cell lysis assay

Cell lysis was evaluated by measuring the release of UV-absorbing materials at 260 nm using a UV/visible spectrophotometer (Jenway 6405, U.K.). Overnight cultures of *L. monocytogenes*, *E. coli*, and *B. cereus* (~1×10^9 CFU/mL) were harvested (4500 g, 15 min, 4 °C), washed three times, and resuspended in PBS (pH 7.4). Cell suspensions were treated with SPI, Fe_3O_4-NPs-SPI, and ZnO-NPs-SPI at the respective MIC of each treatment for the corresponding bacterial strain and incubated at 37 °C for 60-, 120-, and 240-min. Untreated cultures served as controls. Supernatants were collected after centrifugation

(13,400 g, 15 min), and OD_{260} values were recorded to quantify nucleic acid leakage as an indicator of cell lysis (Zhou *et al.* 2008).

Crystal violet uptake

Membrane permeability was evaluated using crystal violet uptake assay. Overnight cultures of *L. monocytogenes*, *E. coli*, and *B. cereus* (~1 × 10^9 CFU/mL) were harvested (4500 g, 15 min, 4 °C), washed three times, and resuspended in PBS (pH 7.4). Cell suspensions were treated with SPI, Fe_3O_4-NPs-SPI, and ZnO-NPs-SPI (at the respective MIC of each treatment for the corresponding bacterial strain), or EDTA (100 µg/mL) and incubated at 37 °C for 1 h. Untreated cultures served as controls. After incubation, cells were centrifuged (9300 g, 5 min), resuspended in PBS containing crystal violet (10 µg/mL), incubated for 10 min, and centrifuged again (13,400 g, 15 min). Absorbance of supernatant was measured at 590 nm using a UV/visible spectrophotometer (Jenway 6405, U.K.), and uptake (%) was calculated relative to the OD of the original dye solution (100%) (Vaara and Vaara 1981).

Cytotoxicity Evaluation

Cell culture conditions

Vero (normal kidney) cell lines, human lung (A549) and colon (HCT116) cancer cell lines obtained from ATCC (USA) were cultured in DMEM supplemented with 10% FBS and maintained at 37 °C under a humidified atmosphere containing 5% CO_2 until use.

MTT cytotoxicity assay

Anticancer activity of SPI, Fe_3O_4-NPs-SPI, and ZnO-NPs-SPI was evaluated using MTT assay (Mosmann1983; Dawoud *et al.* 2022). Vero, A549 and HCT116 cells (1×10^4 cells/well) were seeded in 96-well plates and treated with samples at concentrations ranging from 31.25 to 1000 µg/mL for 72 h, while untreated cells served as controls. After treatment, cells were washed with PBS and incubated with MTT solution (0.5 mg/mL) for 4–5 h. Formazan crystals were dissolved in DMSO, and absorbance was measured at 590 nm using a microplate reader. Cell viability (%) was calculated as,

$$\text{Viability } \% = \frac{\text{Mean OD Treated}}{\text{Mean OD Control}} \times 100 \quad (1)$$

where OD represents optical density. IC_{50} values were derived to quantify cytotoxic activity of each treatment. Selectivity Index (SI) was calculated as IC_{50} (Vero cells) / IC_{50} (cancer cells); SI > 2 indicates selective cytotoxicity toward cancer cells (Rashidi *et al.* 2017).

Caspase 3 and caspase 9 assays

Activities of caspase-3 and caspase-9 in A549 and HCT116 cells were determined after 24 h exposure to IC_{50} concentrations of SPI, Fe_3O_4-NPs-SPI, and ZnO-NPs-SPI. Quantification was performed using commercial human ELISA kits according to the supplier's protocols.

Statistical Analysis

Statistical analyses were performed using IBM SPSS Statistics version 25. Treatment effects were assessed by one-way ANOVA, followed by Tukey's post hoc test for multiple comparisons. Differences were considered statistically significant at $P < 0.05$. All assays were performed in triplicate (n = 3 independent biological replicates).

RESULTS

SDS-PAGE of SPI

The SDS-PAGE profiles of SPI are presented in Fig. 1. The analysis revealed distinct bands corresponding to major soybean storage proteins, β-conglycinin, and glycinin. In high molecular weight region, three bands were observed for the β-conglycinin subunits: α′ (~110 to 120 kDa), α (~90 to 95 kDa), and β (~70 to 75 kDa). The intermediate region displayed prominent bands for glycinin acidic subunits (~50 to 60 kDa), while the lower molecular weight region showed bands for glycinin basic subunits (~30 to 35 kDa). These molecular weight estimations are consistent with previously reported soybean protein profiles, confirming the identity and integrity of SPI.

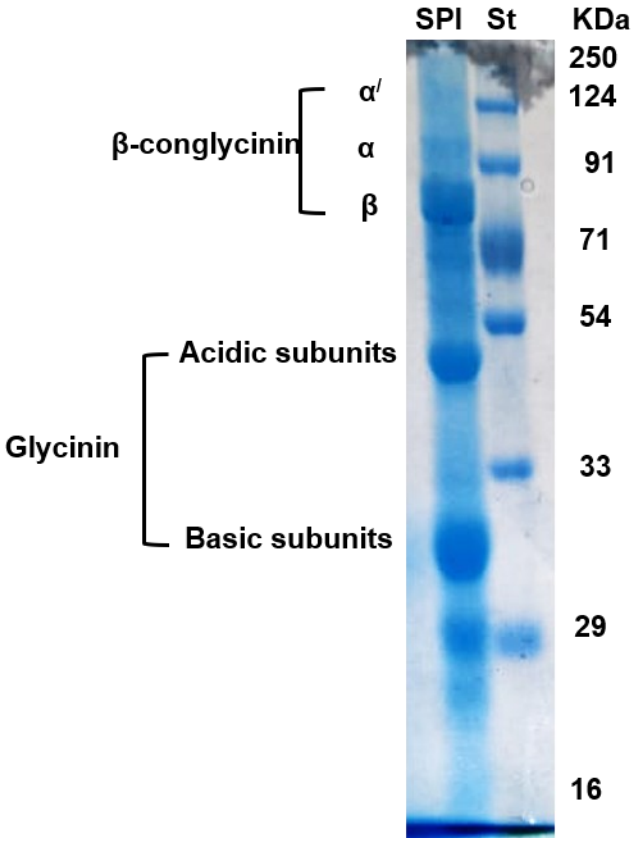

Fig. 1. SDS-PAGE of soy protein isolate compared to protein standard (St)

Characterization of Nanoparticles

TEM analysis revealed that Fe_3O_4-NPs were mainly spherical in shape with relatively smooth surfaces. Their high electron density produced typical dark appearance observed in micrographs (Fig. 2A). Only limited particle aggregation was detected, indicating effective stabilization and surface coating by SPI in the Fe_3O_4-NPs-SPI nanocomposite (Fig. 2D). For ZnO-NPs, the high-resolution TEM analysis (Fig. 3A) was carried out to confirm formation of green synthesized ZnO-NPs. TEM image clearly demonstrated the spherical shape with distinct well grown spherical ZnO nanocrystals were formed with aggregated extra SPI surrounding the nanocrystals are found (Fig. 3D). DLS analysis for Fe_3O_4-NPs and Fe_3O_4-NPs-SPI revealed values of 32 ± 5.2 nm, and 64± 6.7

nm, respectively (Fig. 2B and 2E). Similarly, DLS revealed size of ZnO-NPs was 55 ± 4.8 nm (Fig. 2B), and the size of ZnO-NPs-SPI was 84 ± 6.5 nm (Fig. 3E). XRD pattern of Fe_3O_4-NPs resulted in intense diffraction peaks at 2θ = 19.1°, 30.1°, 35.5°, 43.1°, 53.5°, 57.0°, and 62.7° (Fig. 2C), indexed to (111), (220), (311), (400), (422), (511), and (440) crystallographic planes, respectively, of cubic spinel structure characteristic of magnetite (JCPDS 19-0629).

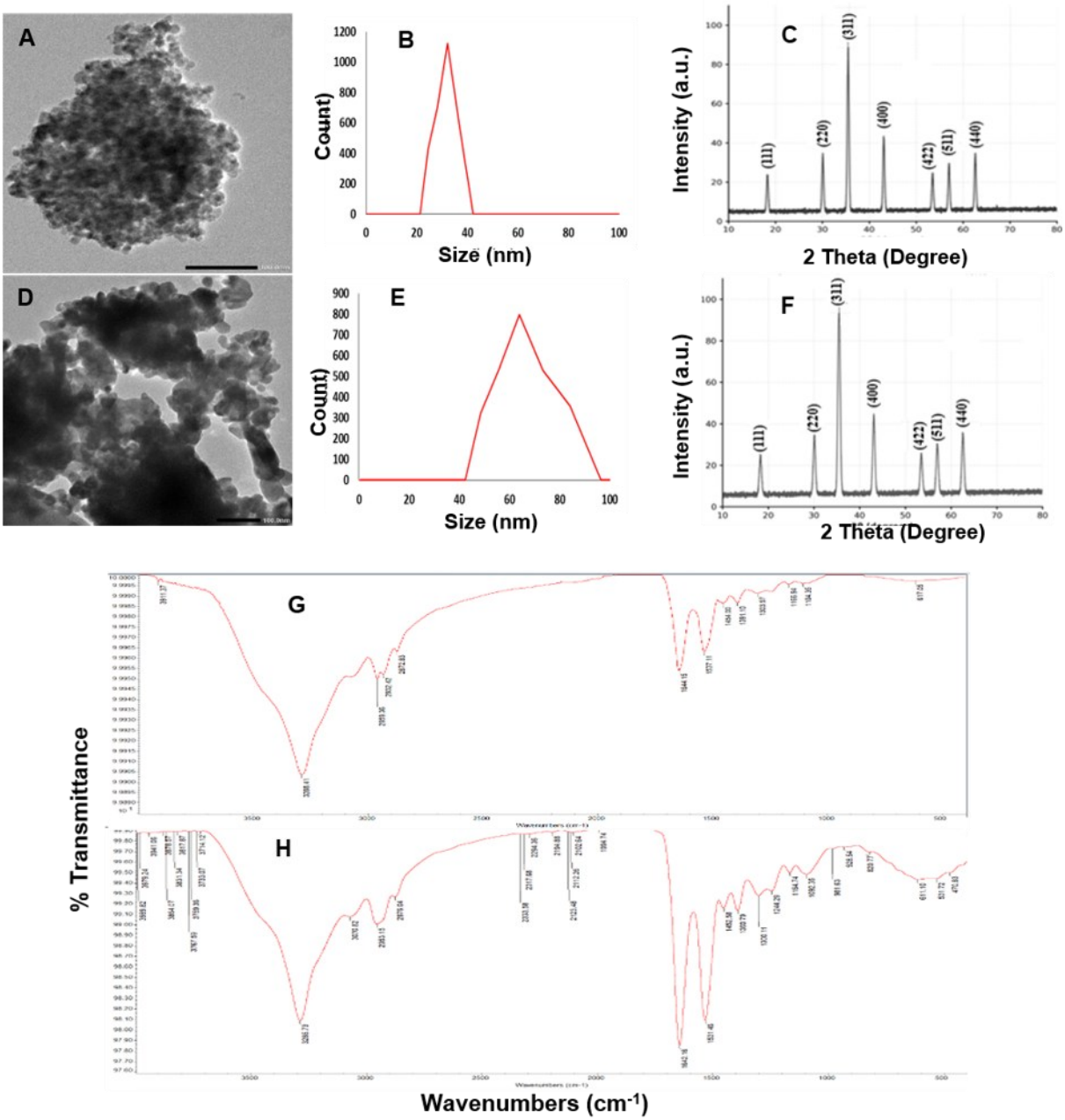

Fig. 2. Characterization of Fe_3O_4-NPs (A) TEM image; (B) DLS particle size distribution; (C) XRD of NPs; (D) TEM image of conjugated Fe_3O-NPs with SPI; (E) DLS particle size distribution of Fe_3O_4-NPs + SPI; (F) XRD of Fe_3O_4-NPs + SPI; (G) FTIR of Fe_3O_4-NPs; and (H) FTIR of Fe_3O_4-NPs + SPI

Fe_3O_4-NPs-SPI maintained characteristic cubic spinel diffraction pattern with peaks at identical 2θ positions (Fig. 2F). The XRD pattern of ZnO-NPs resulted in diffraction peaks at 2θ = 31.85°, 34.55°, 36.35°, 47.69°, 56.75°, 63.09°, and 69.29°

corresponding to lattice planes (100), (002), (101), (102), (110), (103), and (200), respectively (Fig. 3C). ZnO-NPs-SPI conjugation maintained characteristic cubic spinel diffraction pattern with peaks at identical 2θ positions (Fig. 3F).

FTIR was acquired in wavenumber range of 4000 to 500 cm^{-1} with 4 cm^{-1} resolution, and results are compiled in (Figs. 2G and 2H). Fe_3O_4-NPs-SPI exhibited the O–H stretching band at 3285.7 cm^{-1} and H–O–H bending at 1642.2 cm^{-1}. Diagnostic Fe–O vibrational modes of the spinel structure appeared as prominent absorbance band at 617.0 cm^{-1}. In spectrum of Fe_3O_4-NPs-SPI the function groups were assigned. It is clear from tables and graphs that there was a shifting in some peaks due to the loading of soy bean protein isolate (SPI) compound onto magnetite nanoparticles.

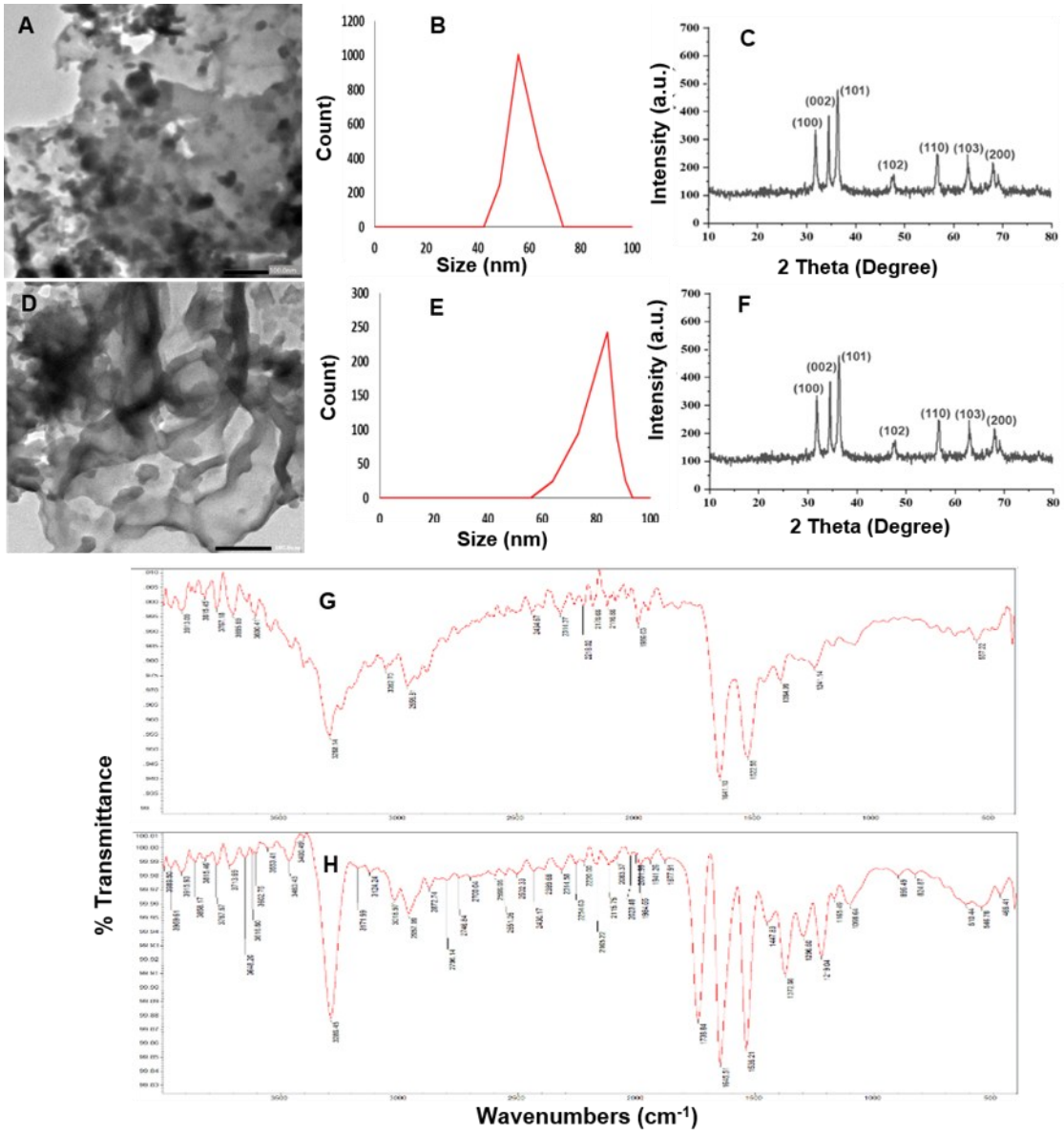

Fig. 3. Characterization of ZnO-NPs: (A) TEM image of ZnO-NPs; (B) DLS particle size distribution of ZnO NPs; (C) XRD of ZnO-NPs; (D) TEM image of conjugated ZnO-NPs with SPI; (E) DLS particle size distribution of ZnO-NPs with SPI; (F) XRD of ZnO-NPs with SPI; (G) FTIR of ZnO-NPs; and (H) FTIR of ZnO-NPs with SPI

The FTIR absorbance spectra in (Fig. 3G and 3H) revealed a sharp absorbance peak at 557.2 cm^{-1}, which is the characteristic ZnO peak, which affirmed green synthesis of ZnO-NPs *via* ascorbic acid. Functional group of ZnO-NPs green synthesis using ascorbic acid was detected by FTIR analysis. The peak at 3288.1 cm^{-1} corresponded to the OH-hydroxyl group of alcohols (related to ascorbic acid). FTIR spectra showed bands at 2959.8 to 3052.7 cm^{-1} that can be attributed to C–H stretching vibrations, while signals at 1600 to 1550 cm^{-1} corresponded to protein amide groups. Peaks between 1000 and 950 cm^{-1} were associated with C–N and C–H bending of amine-containing phytochemicals. Following nanoparticle formation, several bands shifted to lower wavenumbers and decreased in intensity, indicating the involvement of protein carbonyl and amino groups in metal binding, nanoparticle coating, and stabilization against aggregation. The absence of additional diffraction peaks beyond those indexed to the cubic spinel (Fe_3O_4) and wurtzite (ZnO) structures indicates high phase purity of the synthesized nanoparticles.

Collectively, the convergent multi-method evidence comprising FTIR amide band redshifts (protein amide signals at 1600 to 1550 cm^{-1}), DLS-measured hydrodynamic size increases (Fe_3O_4-NPs: 32 to 64 nm; ZnO-NPs: 55 to 84 nm), TEM-confirmed morphological envelope changes, and XRD-verified crystallinity retention of nanoparticle cores — provided robust and consistent support for successful SPI conjugation and surface stabilization of both nanocomposites, in line with established multi-method characterization standards for protein-coated nanoparticles (Monopoli *et al.* 2011; Mbeh *et al.* 2015). Zeta potential measurement, which provides complementary electrokinetic evidence of surface charge modification accompanying protein adsorption, constitutes a valuable additional technique; its incorporation is recommended in future characterization studies to provide further electrokinetic confirmation of the protein–nanoparticle interface.

Antibacterial Activity

Agar well diffusion

The antibacterial assay results demonstrate that soybean protein isolate (SPI) exhibited selective inhibitory activity, with pronounced effects against *B. cereus* and *L. monocytogenes*, but negligible inhibition of *E. coli* at lower concentrations (Table 1). Notably, SPI alone achieved inhibition zones up to 43 mm against *L. monocytogenes* and 40 mm against *B. cereus* at 1000 µg/mL, while activity against *E. coli* was only evident at higher concentrations (≥500 µg/mL). Conjugation of SPI with Fe_3O_4-NPs markedly enhanced activity against *E. coli*, producing inhibition zones of 30 to 41 mm across tested concentrations, while also sustaining moderate activity against *L. monocytogenes* and gradually increasing inhibition of *B. cereus*. In contrast, ZnO-NPs exhibited broad-spectrum efficacy, with consistent inhibition across all tested bacteria. At 1000 µg/mL, ZnO-NPs-SPI achieved inhibition zones of 38 mm (*L. monocytogenes*), 41 mm (*E. coli*), and 38 mm (*B. cereus*), highlighting its superior synergistic effect compared to SPI alone or Fe_3O_4-NPs-SPI.

Minimum inhibitory concentration

The results clearly demonstrated that nanoformulation significantly enhanced the antibacterial activity of SPI (Fig. 4A). Against *L. monocytogenes*, SPI alone exhibited a high MIC value of 31.2 µg/mL, whereas both Fe_3O_4-NPs-SPI and ZnO-NPs-SPI reduced the MIC to 3.9 µg/mL, representing approximately an 8-fold improvement. A similar trend was observed for *E. coli*, where the MIC decreased from 31.2 µg/mL (SPI) to 3.9 µg/mL for both nanoformulations.

Table 1. Antibacterial Activity of SPI and its Nanoparticle Conjugates (Fe_3O_4-NPs-SPI and ZnO-NPs-SPI) against *L. monocytogenes*, *E. coli*, and *B. cereus* at Different Concentrations

Tested Materials	Concentration (µg/mL)	Inhibition Zone Diameter (mm)±SD		
		L. monocytogenes	*E. coli*	*B. cereus*
SPI	31.25	0 ±0 ^{g}	0 ±0 ^{h}	24 ±0.57^{f}
	62.5	0 ±0 ^{g}	0 ±0 ^{h}	29 ±1.15^{e}
	125	35 ±1.15 ^{cd}	0 ±0 ^{h}	35 ±1.52^{cd}
	250	37 ±2.5 ^{bcd}	0 ±0 ^{h}	36 ±1.73^{bcd}
	500	40 ±2.3 ^{ab}	39 ±2.08 ^{ab}	37 ±1.15^{abc}
	1000	43 ±1.73 ^{a}	40 ±1 ^{ab}	40 ±0.57^{a}
Fe_3O_4-NPs-SPI	31.25	27 ±2.3^{f}	30 ±0 ^{g}	0 ±0 ^{k}
	62.5	30 ±2.6 ^{e}	31 ±1 ^{fg}	9 ±0.7 ^{j}
	125	33 ±3$^{cd\ e}$	33 ±2.6^{def}	13 ±2.12 ^{i}
	250	33 ±3.5^{cde}	35 ±1.52^{cde}	18 ±0.7 ^{h}
	500	35 ±4 ^{cd}	40 ±0.57 ^{ab}	23 ±1.41 ^{g}
	1000	37 ±2.5 ^{bcd}	41 ±1.41 ^{a}	30 ±2.12^{e}
ZnO-NPs-SPI	31.25	26 ±2.3 ^{f}	32 ±2 ^{fg}	0 ±0 ^{k}
	62.5	27 ±3 ^{f}	33 ±1.52^{def}	25 ±0.7$^{f\ g}$
	125	29 ±1.15 ^{e}	35 ±0de	26 ±3.5^{f}
	250	31 ±3.6 ^{ef}	36 ±1.73^{cd}	30 ±3^{e}
	500	35 ±0.57 ^{cd}	38 ±2^{bc}	34 ±0.7^{d}
	1000	38 ±1.73 ^{bc}	41 ±3.6 ^{a}	38 ±0.57^{a}

Means with different superscripts in the same column are significantly different (* P <0.05) Tukey HSD test.

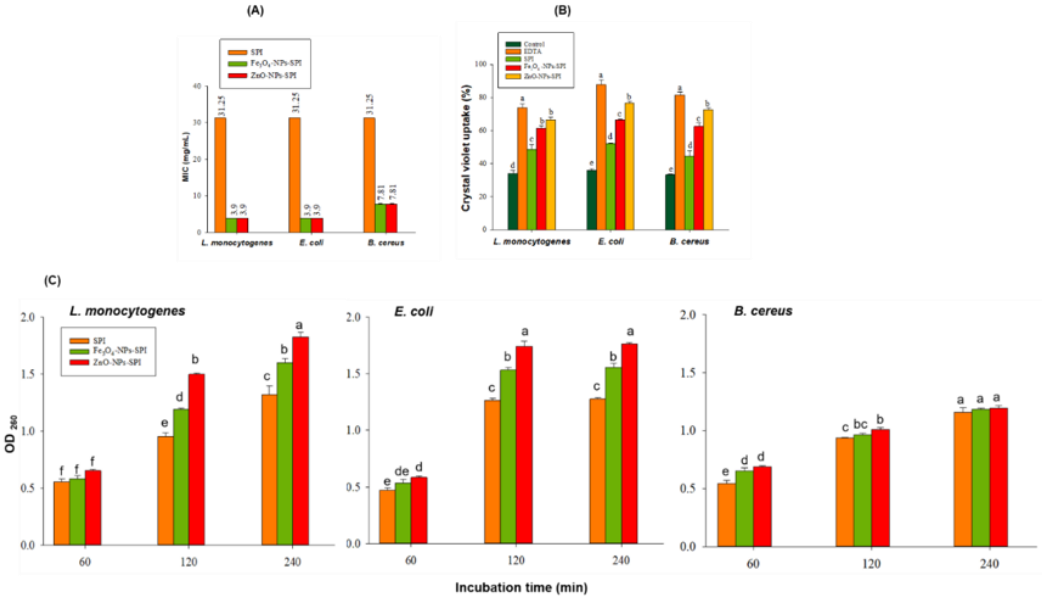

Fig. 4. Antibacterial activity and membrane-disruptive effects of SPI and its nanoparticle-based formulations against foodborne pathogenic bacteria: (A) MIC values of (µg mL^{-1}) of SPI, Fe_3O_4-NPs-SPI, and ZnO-NPs-SPI against *L. monocytogenes*, *E. coli*, and *B. cereus*; (B) Crystal violet uptake (%) by *L. monocytogenes*, *E. coli*, and *B. cereus* following treatment with SPI, Fe_3O_4-NPs-SPI, and ZnO-NPs-SPI at their respective MIC values, compared with untreated control and EDTA-treated cells, indicating changes in cell membrane permeability; (C) Release of intracellular materials measured as absorbance at 260 nm (OD_{260}) in *L. monocytogenes*, *E. coli*, and *B. cereus* after exposure to SPI, Fe_3O_4-NPs-SPI, and ZnO-NPs-SPI at MIC, reflecting bacterial cell lysis and membrane damage. Data are presented as mean ± SD. Different superscript letters indicate significant differences among treatments within each bacterial species according to Tukey's HSD test ($P < 0.05$)

In contrast, *B. cereus* showed a different response pattern, with identical MIC values of 7.81 µg/mL for SPI, Fe_3O_4-NPs-SPI, and ZnO-NPs-SPI, indicating no enhancement in antibacterial activity upon nanoformulation.

Bacterial growth curve

The antibacterial activity of SPI and its nanoparticle conjugates was evaluated against *L. monocytogenes*, *E. coli*, and *B. cereus* by monitoring bacterial growth (OD_{600}) over 24 h incubation (Fig. 5).

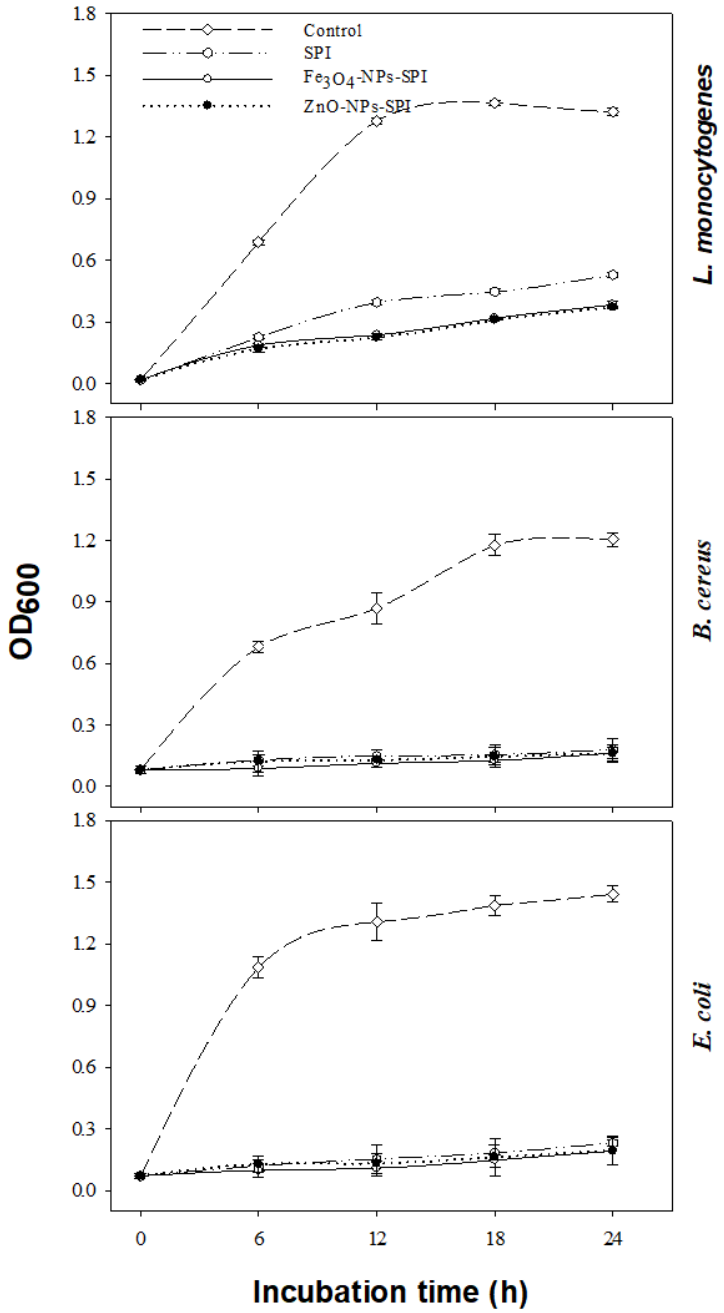

Fig. 5. Growth inhibition of *L. monocytogenes*, *B. cereus*, and *E. coli* monitored by optical density at 600 nm (OD_{600}) during 24 h incubation following treatments with soybean protein isolate (SPI), Fe_3O_4-NPs -SPI and ZnO-NPs-SPI at 1MIC compared to untreated control cultures

For *L. monocytogenes*, untreated controls exhibited rapid proliferation, reaching OD_{600} values of 1.28 at 12 h and 1.367 at 18 h before stabilizing at 1.323 after 24 h. In contrast, SPI treatment significantly reduced growth, with OD_{600} values of 0.395 at 12 h and 0.530 at 24 h. Conjugation with Fe_3O_4-NPs enhanced inhibition, maintaining OD_{600} below 0.383 at 24 h, while ZnO-NPs-SPI demonstrated the strongest effect, limiting OD_{600} to 0.371.

For *E. coli*, control cultures showed unrestricted growth, rising from 1.087 at 6 h to 1.442 at 24 h. SPI markedly suppressed proliferation, maintaining OD_{600} at 0.231 after 24 h. Fe_3O_4-NPs -SPI and ZnO-NPs-SPI treatments produced even stronger inhibition, restricting OD_{600} to ~0.192–0.193 at 24 h, with values consistently below 0.20 throughout incubation.

For *B. cereus*, control cultures increased steadily from 0.68 at 6 h to 1.20 at 24 h. SPI treatment reduced growth to 0.179 at 24 h, while Fe_3O_4-NPs-SPI and ZnO-NPs-SPI further suppressed proliferation, maintaining OD_{600} at 0.163 and 0.161, respectively. Both nanoparticle conjugates restricted bacterial growth consistently, confirming their synergistic enhancement of SPI's intrinsic antibacterial activity.

Crystal violet uptake

The crystal violet uptake assay revealed a clear increase in membrane permeability across all tested microorganisms following treatment, with notable differences among treatments and species (Fig. 4B). EDTA treatment resulted in the highest crystal violet uptake percentages in all strains, reaching 73.7% in *L. monocytogenes*, 87.6% in *E. coli*, and 81.4% in *B. cereus*. This substantial increase compared to the control (≈33% to 36%) confirms the strong membrane-disrupting effect of EDTA, likely due to its chelating action on divalent cations that stabilize the cell envelope. SPI alone induced a moderate increase in uptake, indicating a partial effect on membrane integrity. However, the incorporation of Fe_3O_4-NPs and ZnO-NPs significantly enhanced this effect. The ZnO-NPs-SPI treatment exhibited the highest uptake among the composite systems (66.37%, 76.58%, and 72.46% for *L. monocytogenes*, *E. coli*, and *B. cereus*, respectively), followed by Fe_3O_4-NPs-SPI. This suggests a synergistic interaction between SPI and nanoparticles, improving membrane permeability more effectively than SPI alone. Among the tested organisms, *E. coli* consistently showed the highest susceptibility, while *L. monocytogenes* and *B. cereus* exhibited relatively lower but comparable responses. The low standard deviation values across treatments indicate good experimental reproducibility.

Cell lysis

The absorbance values (OD_{260}) demonstrate progressive leakage of nucleic acids, confirming membrane disruption and lysis across all tested bacteria (Fig. 4C). Statistical analysis revealed highly significant differences among treatments and incubation times ($P < 0.05$). In *L. monocytogenes*, ZnO-NPs-SPI induced the earliest and most pronounced lysis, reaching 1.50 at 120 min and sustaining the highest release (1.829) at 240 min, significantly exceeding SPI (1.323) and Fe_3O_4-NPs-SPI (1.602). Similarly, in *E. coli*, ZnO-NPs-SPI triggered rapid envelope destabilization (0.584 at 60 min), with maximal lysis plateauing at 1.763 by 240 min, surpassing SPI (1.279) and Fe_3O_4-NPs-SPI (1.558) with clear statistical separation. For *B. cereus*, ZnO-NPs-SPI again produced the strongest effect (0.690 at 60 min; 1.196 at 240 min), though differences relative to SPI and Fe_3O_4-NPs-SPI were less pronounced, consistent with species-specific variability in susceptibility. Across

all species, Fe_3O_4-NPs conjugation consistently enhanced lysis compared to SPI alone, but ZnO-NPs conjugation yielded the most potent and reproducible bacteriolytic activity.

In-vitro Cytotoxicity, IC_{50} Analysis, and Caspase-3 and -9 Levels

The *in vitro* cytotoxic profiles of SPI, Fe_3O_4-NPs-SPI, and ZnO-NPs-SPI were evaluated against A549 and HCT116 cell lines, revealing a distinct, dose-dependent reduction in cell viability across concentrations ranging from 31.25 to 1000 µg/mL (Fig. 6A). The ZnO-NPs-SPI demonstrated the highest potency, significantly decreasing cell viability even at lowest tested concentration (31.25 µg/mL) and yielding the lowest half-maximal inhibitory concentration (IC_{50}) values of 27.8 µg/mL for A549 and 31.25 µg/mL for HCT116 cells. In comparison, the Fe_3O_4-NPs-SPI showed intermediate toxicity with IC_{50} values of 53.87 µg/mL (A549) and 62.5 µg/mL (HCT116), while unmodified SPI proved to be the least toxic, requiring much higher concentrations of 142 µg/mL and 227 µg/mL to achieve 50% growth inhibition, respectively (Fig. 6B).

To investigate underlying mechanism of cell death induced by the formulations, the levels of key apoptotic enzymes Caspase 3 and Caspase 9 were evaluated in both A549 and HCT116 cell lines. As shown in Fig. 6C. treatment with SPI, Fe_3O_4-NPs-SPI, and ZnO-NPs-SPI triggered a significant, formulation-dependent upregulation of both caspases compared to untreated control group.

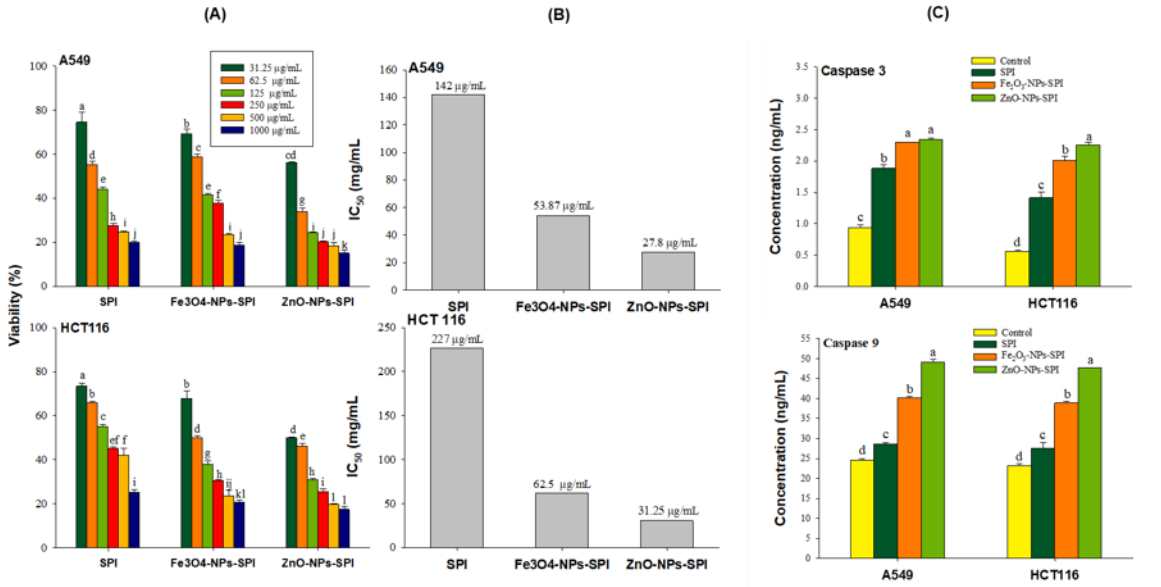

Fig. 6. Cytotoxic and apoptotic effects of SPI and its nanoparticle composites on human cancer cell lines: (A) Dose-dependent cytotoxicity profiles of SPI, Fe_3O_4-NPs-SPI, and ZnO-NPs-SPI against human cancer cell lines A549 and HCT116 following treatment with concentrations ranging from 31.25 to 1000 µg/mL. Cell viability is expressed as percentage relative to untreated controls; (B) Corresponding IC_{50} values (µg/mL) of SPI and its nanoformulations against A549 and HCT116 cells; (C) Effects of SPI, Fe_3O_4-NPs-SPI, and ZnO-NPs-SPI on the concentration of caspase-3 and caspase-9 in A549 and HCT116 cell lines, indicating apoptosis induction. Data are presented as mean ± standard deviation (SD). Means or bars bearing different lowercase letters (a–d) indicate significant differences among treatments within the same cell line according to one-way ANOVA followed by Tukey's HSD post hoc test ($P < 0.05$)

In case of Caspase 3, exposure to the Fe_3O_4-NPs-SPI, and ZnO-NPs-SPI resulted in the sharpest increase in concentration, with ZnO-NPs-SPI and Fe_3O_4-NPs-SPI driving

levels up to approximately 2.3 ng/mL in A549 cells and over 2.0 ng/mL in HCT116 cells. For Caspase 9, a clear step-wise, statistically significant increase was observed across the groups. The ZnO-NPs-SPI stimulated the highest production of Caspase 9, reaching peak concentrations of roughly 49 ng/mL in A549 and 48 ng/mL in HCT116 cells.

As shown in Table 2, all tested materials exhibited cytotoxic activity against both A549 and HCT116 cancer cells, with the nanoformulated preparations showing substantially greater potency than SPI alone. SPI displayed IC_{50} values of 142 and 277 µg/mL against A549 and HCT116 cells, respectively, whereas incorporation with Fe_3O_4-NPs markedly reduced the IC_{50} values to 53.9 and 62.5 µg/mL. The strongest cytotoxic activity was observed for ZnO-NPs-SPI, with IC_{50} values of 27.8 µg/mL against A549 and 31.2 µg/mL against HCT116 cells. In contrast, the IC_{50} values against normal Vero cells were relatively high (555, 520, and 532 µg/mL for SPI, Fe_3O_4-NPs-SPI, and ZnO-NPs-SPI, respectively), indicating lower cytotoxicity toward normal cells. Consistent with these findings, the selectivity index (SI) values demonstrated a clear improvement following nanoformulation. SPI exhibited SI values of 3.90 and 2.00 against A549 and HCT116 cells, respectively, while Fe_3O_4-NPs-SPI increased the SI to 9.65 and 8.30. ZnO-NPs-SPI showed the highest selectivity, with SI values of 19.13 for A549 and 17.00 for HCT116 cells.

Table 2. Cytotoxic Activity (IC_{50}) and Selectivity Index (SI) of SPI, Fe_3O_4-NPs-SPI, and ZnO-NPs-SPI against A549 and HCT116 Cancer Cells after 72 h Exposure

Tested Materials	**IC_{50} (µg/mL)**		
	Vero	A549	HCT116
SPI	555	142	277
Fe_3O_4-NPs-SPI	520	53.87	62.5
ZnO-NPs-SPI	532	27.8	31.25
	Selectivity Index		
SPI		3.9	2
Fe_3O_4-NPs-SPI		9.65	8.3
ZnO-NPs-SPI		19.13	17

DISCUSSION

The present study demonstrated that conjugation of SPI with Fe_3O_4 and ZnO nanoparticles significantly enhanced its biological activities. Characterization analyses confirmed the successful synthesis and stabilization of both nanoparticle systems by SPI, as evidenced by TEM, DLS, XRD, and FTIR results. The observed increase in particle size following conjugation further supports the formation of protein-coated nanostructures, which likely improved nanoparticle stability and bioactivity (Mourad *et al.* 2025). The FTIR-observed shifts in carbonyl and amine-related bands suggest that SPI binds to the Fe_3O_4-NP and ZnO-NP surfaces predominantly through non-covalent electrostatic and coordinate interactions rather than covalent bonding. Quantitative determination of binding affinity and stoichiometry (*e.g.*, *via* adsorption isotherms or isothermal titration calorimetry) was outside the scope of the present study and is recommended for future investigation.

The retention of characteristic XRD diffraction patterns after SPI conjugation indicates preserved crystalline structure over the assay period; however, time-resolved quantification of nanoparticle dissolution and metal-ion release (for instance, by ICP-

OES/ICP-MS across extended incubation periods and physiologically relevant media) was not performed in this study and is recommended as future work to fully characterize long-term stability and secondary toxicity risk.

The antibacterial results revealed that nanoformulation markedly improved the efficacy of SPI against both Gram-positive and Gram-negative bacteria. Reduction in MIC values and the larger inhibition zones observed for Fe_3O_4-NPs-SPI and ZnO-NPs-SPI indicate a synergistic interaction between SPI and the nanoparticles. This enhancement may be attributed to nanoscale size of the particles, which facilitates close interaction with bacterial cell surfaces and promotes membrane damage (Modi *et al.* 2023). The crystal violet uptake and cell lysis assays further confirmed that the antibacterial mechanism involves disruption of membrane integrity, leading to increased permeability, and leakage of intracellular components (Jeyanthi *et al.* 2021). Similar mechanisms have been reported for metal oxide nanoparticles, where oxidative stress generation and membrane destabilization contribute to bacterial cell death (Mammari *et al.* 2022). One limitation of this study is that the cell lysis assay was limited to a 4 h incubation period; therefore, the long-term progression of membrane leakage and sustained bactericidal effects remain to be investigated in future studies

Among the tested formulations, ZnO-NPs-SPI consistently exhibited superior antibacterial activity. ZnO-NPs are known to possess strong antimicrobial properties because of their ability to generate reactive oxygen species (ROS), release Zn^{2+} ions, and interact directly with microbial membranes (Li *et al.* 2020). The enhanced crystal violet uptake and nucleic acid leakage observed in the present study support these mechanisms and explain the greater susceptibility of *E. coli*, *L. monocytogenes*, and *B. cereus* to ZnO-NPs-SPI treatment.

In the present study, the antimicrobial mechanisms of SPI–nanoparticle conjugates were primarily inferred from crystal violet uptake and nucleic acid leakage assays, which provided indirect but consistent evidence of membrane permeability enhancement and bacteriolysis. These findings align with established methodologies for evaluating antibacterial agents, yet we acknowledge that they do not fully capture the complexity of nanoparticle–bacteria interactions. Direct mechanistic validation remains an important future direction. Specifically, incorporation of ROS quantification (*e.g.*, DCFH-DA fluorescence), TEM visualization of treated cells, and intracellular enzyme leakage assays would provide ultrastructural and biochemical confirmation of oxidative stress and cytoplasmic damage. Furthermore, zeta potential analysis could complement FTIR and DLS data by offering electrokinetic evidence of protein–nanoparticle interactions at the bacterial surface. Collectively, these additional approaches will enrich the mechanistic understanding of SPI-based nanocomposites, ensuring a more comprehensive evaluation of their antibacterial activity.

Another limitation of this study is that the potential for bacterial resistance development against SPI–nanoparticle conjugates were not evaluated. Although nanoparticle-based antimicrobials often act through multifactorial mechanisms such as membrane disruption and oxidative stress, adaptive responses including efflux pump activation or biofilm formation remain possible. Future work should therefore include serial passage experiments and genomic analyses to assess the likelihood of resistance emergence during prolonged exposure.

The cytotoxicity studies also demonstrated a clear dose-dependent reduction in cancer cell viability. The substantially lower IC_{50} values of ZnO-NPs-SPI and Fe_3O_4-NPs-SPI compared with SPI alone indicate that nanoparticle incorporation significantly

increased anticancer potency. ZnO-NPs-SPI showed the greatest cytotoxic effect against both A549 and HCT116 cells, suggesting enhanced cellular uptake and intracellular activity (Anjum *et al.* 2021). Previous studies have reported that ZnO nanoparticles selectively induce oxidative stress in cancer cells, resulting in mitochondrial dysfunction and activation of programmed cell death pathways (Li *et al.* 2024).

The enhanced cytotoxicity and selectivity observed following nanoformulation may be attributed to the ability of Fe_3O_4 and ZnO nanoparticles to improve the cellular delivery and biological availability of SPI-derived bioactive components. Compared with SPI alone, both nanoformulations produced considerably lower IC_{50} values in A549 and HCT116 cells, with ZnO-NPs-SPI exhibiting the greatest potency. The particularly high SI values of ZnO-NPs-SPI (19.13 and 17.00 for A549 and HCT116, respectively) indicate a pronounced preference for cancer cells over normal Vero cells, whereas Fe_3O_4-NPs-SPI also demonstrated substantial selectivity (SI = 9.65 and 8.30). These findings suggest that nanoparticle incorporation may enhance the anticancer efficacy of SPI while maintaining comparatively low toxicity toward normal cells.

Our focus was to evaluate soy protein isolate (SPI) as a biocompatible carrier and to highlight the synergistic enhancement achieved through conjugation, rather than to re-establish the well-documented intrinsic activities of ZnO nanoparticles and Fe_3O_4 nanoparticles. Nevertheless, future studies should incorporate direct comparisons between nanoparticle-only treatments and SPI–nanoparticle conjugates to disentangle additive versus synergistic contributions and provide clearer mechanistic insights.

The significant elevation of caspase-3 and caspase-9 levels following treatment provides strong evidence that apoptosis is a major mechanism underlying anticancer activity of synthesized nanocomposites (Safa *et al.* 2025). Caspase-9 is a key initiator of the intrinsic mitochondrial apoptotic pathway, while caspase-3 functions as a major executioner caspase responsible for cellular dismantling (Avrutsky and Troy 2021). The pronounced activation of both enzymes, particularly in the ZnO-NPs-SPI-treated groups, suggests that mitochondrial-mediated apoptosis plays a central role in cancer cell death. Enhanced apoptotic response may result from nanoparticle-induced oxidative stress, mitochondrial membrane depolarization, and subsequent activation of the caspase cascade (Cameron *et al.* 2022).

The apoptotic mechanism was evaluated through caspase-3 and caspase-9 activation assays, which were conducted at a single time point (24 h) using IC_{50} concentrations of SPI–nanoparticle conjugates. While these results provide a clear snapshot of apoptosis induction, they represent a limited view of the temporal and dose-dependent dynamics of caspase activation. Future studies should incorporate kinetic profiling at multiple time points (e.g., 6, 12, 24, and 48 h) to capture the progression of apoptotic signaling, as well as dose–response analysis to determine threshold and saturation effects. Such approaches, complemented by additional apoptosis markers (*e.g.*, Annexin V staining, TUNEL assay), would provide a more comprehensive mechanistic understanding of how SPI–nanoparticle conjugates trigger cell death pathways. These enhancements will strengthen the evidence base for apoptosis-mediated cytotoxicity and clarify whether the observed effects are early, sustained, or secondary responses to nanoparticle exposure.

Overall, the findings demonstrate that SPI serves not only as a biocompatible stabilizing matrix but also as an effective carrier that enhances the biological performance of Fe_3O_4-NPs and ZnO-NPs. Synergistic combination of SPI with metal oxide nanoparticles, especially ZnO, resulted in improved antibacterial and anticancer activities

through mechanisms involving membrane disruption and apoptosis induction. These multifunctional properties highlight the potential application of SPI-based nanocomposites in pharmaceutical, biomedical, and food preservation fields. The pH-dependent stability and release kinetics of the nanocomposites were not evaluated in this study; all bioassays were conducted at physiological pH (7.4). Given the relevance of this parameter to food-system and oral biomedical applications, future work will assess conjugate stability and controlled-release behavior across the gastric-to-intestinal pH range.

CONCLUSIONS

1. Soy protein isolate-based nanocomposites containing Fe_3O_4 and ZnO nanoparticles were successfully synthesized and characterized, confirming effective nanoparticle conjugation and physicochemical stability.
2. Nanoformulation significantly enhanced the antibacterial activity of SPI against both Gram-positive and Gram-negative bacteria, particularly *L. monocytogenes* and *E. coli* through increased membrane disruption and bacteriolytic effects.
3. Among the tested formulations, ZnO-NPs-SPI exhibited the highest biological activity, demonstrating superior antimicrobial efficacy and the lowest IC_{50} values against A549 and HCT116 cancer cell lines.
4. The significant activation of caspase-3 and caspase-9 in treated cancer cells confirmed that the cytotoxic effect of ZnO-NPs-SPI was mediated through apoptosis.
5. The combined findings demonstrate that SPI-based nanocomposites possess multifunctional antimicrobial and anticancer properties, supporting their potential for biomedical and food-related applications.

ACKNOWLEDGMENTS

The authors gratefully acknowledge the Deanship of Scientific Research, University of Hail, Saudi Arabia, for financial support through project number RG-23 244.

Conflict of Interest

The authors declare that they have no competing financial interests or personal relationships that could have appeared to influence the work reported in this paper.

Use of Generative AI

The authors used Microsoft Copilot solely to assist with English language editing and improvement of grammar, wording, and writing clarity during manuscript preparation. All scientific content, data analysis, interpretation of the results, conclusions, and the final version of the manuscript were prepared, verified, and approved by the authors. Microsoft Copilot was not used to generate or modify figures, graphs, diagrams, or images.

REFERENCES CITED

Abd El-Halim, M. D., Osman, A., Ibrahim, M. A., El-Azab, M. M., El-Saber, M. M., Ismail, S. H., Roshdy, T., Sitohy, M., and Sitohy, B. (2026). "Green-synthesized rhein-selenium nanoparticles exhibit potent and highly selective anticancer activity against colon cancer *via* apoptosis and gene regulation," *Front. Chem.* 14, article 1727890. https://doi.org/10.3389/fchem.2026.1727890

Abdel-Hamid, M., Goda, H.A., De Gobba, C., Jenssen, H., and Osman, A. (2016). "Antibacterial activity of papain hydrolysed camel whey and its fractions," *Int. Dairy J.* 61, 91-98. https://doi.org/10.1016/j.idairyj.2016.04.004

Abdel-Hamid, M., Romeih, E., Saporito, P., Osman, A., Mateiu, R.V., Mojsoska, B., and Jenssen, H. (2020). "Camel milk whey hydrolysate inhibits growth and biofilm formation of *Pseudomonas aeruginosa* PAO1 and methicillin-resistant *Staphylococcus aureus*," *Food Con.* 111, article 107056. https://doi.org/10.1016/j.foodcont.2019.107056

Almutairi, H. H., Aboelftoh, A., El-Beltagi, H. S., Wahdan, K. M., Ahmed, A. R., Osman, A., Ismail, A. M., and El-Maati, M. F. A. (2025). "Multifaceted biological activities of ethanolic guava leaf extract: Antioxidant, antiviral, antibacterial, and anticancer effects," *Waste Biomass Valori.* 1-14. https://doi.org/10.1007/s12649-025-03367-0

Anjum, S., Hashim, M., Malik, S. A., Khan, M., Lorenzo, J. M., Abbasi, B. H., and Hano, C. (2021). "Recent advances in zinc oxide nanoparticles (ZnO NPs) for cancer diagnosis, target drug delivery, and treatment," *Cancers* 13, article 4570. https://doi.org/10.3390/cancers13184570

Avrutsky, M. I., and Troy, C. M. (2021). "Caspase-9: a multimodal therapeutic target with diverse cellular expression in human disease," *Front. Pharmacol.* 12, artucke 701301. https://doi.org/10.3389/fphar.2021.701301

Cameron, S. J., Sheng, J., Hosseinian, F., and Willmore, W. G. (2022). "Nanoparticle effects on stress response pathways and nanoparticle–protein interactions," *Int. J. Mol. Sci.* 23, 7962.

Chen, L., Ramezan, Y., Pourramezan, H., Najafi, A., Kamkari, A., Goksen, G., Huang, Z., and Zhang, W. (2025). "Soy protein isolate (spi)-based films/coatings for food packaging: Research progress on properties and applications," *Compr. Rev. Food Sci. Food Saf.* 24, article e70181. https://doi.org/10.1111/1541-4337.70181

Dawoud, N. T., El-Fakharany, E. M., Abdallah, A. E., El-Gendi, H., and Lotfy, D. (2022). "Synthesis, and docking studies of novel heterocycles incorporating the indazolylthiazole moiety as antimicrobial and anticancer agents," *Sci. Rep.* 12, article 3424. https://doi.org/10.21203/rs.3.rs-1153610/v1

El-Beltagi, H., Osman, A., Rezk, A., Eid, W., Shehata, W., Elakkad, H., Alhajri, A., El-Masry, R., Ahmed, A., and El-Sayed, A. (2025). "Biosynthesis of silver nanoparticles using bitter apple seed extract: Aanticancer and antibacterial activities," *Waste Biomass Valori.* 2025, 1–13. https://doi.org/10.1007/s12649-025-03108-3

El-Beltagi, H. S., Ragab, M., Osman, A., El-Masry, R. A., Alwutayd, K. M., Althagafi, H., Alqahtani, L. S., Alazragi, R. S., Alhajri, A. S., and El-Saber, M. M. (2024a). "Biosynthesis of zinc oxide nanoparticles *via* neem extract and their anticancer and antibacterial activities," *PeerJ.* 12, article e17588. https://doi.org/10.7717/peerj.17588

El-Beltagi, H. S., Rageb, M., El-Saber, M. M., El-Masry, R. A., Ramadan, K. M., Kandeel, M., Alhajri, A. S., and Osman, A. (2024b). "Green synthesis,

characterization, and hepatoprotective effect of zinc oxide nanoparticles from *Moringa oleifera* leaves in CCl_4-treated albino rats," *Heliyon* 10(9), article e30627. https://doi.org/10.1016/j.heliyon.2024.e30627

El-Saber, M. M., Mahdi, A. A., Hassan, A. H., Farroh, K. Y., and Osman, A. (2021). "Effects of magnetite nanoparticles on physiological processes to alleviate salinity induced oxidative damage in wheat," *J. Sci. Food Agric.* 101, 5550-5562. https://doi.org/10.1002/jsfa.11206

Elshafie, H. S., Osman, A., El-Saber, M. M., Camele, I., and Abbas, E. (2023). "Antifungal activity of green and chemically synthesized ZnO nanoparticles against *Alternaria citri*, the causal agent citrus black rot," *Plant Pathol. J.* 39, article 265. https://doi.org/10.5423/ppj.oa.02.2023.0035

Enan, G., El-Wafa, N. A., El-Saber, M. M., Osman, A., Abdel-Shafi, S., and Sitohy, M. (2026). "*Salvia officinalis* extract–conjugated magnetite and selenium nanocomposites showed enhanced antibacterial and anti-biofilm activity against multidrug-resistant pathogens," *Sci. Rep.* 16, article 9201. https://doi.org/10.1038/s41598-026-53471-x

Farid, N., Waheed, A., and Motwani, S. (2023). "Synthetic and natural antimicrobials as a control against food borne pathogens: A review," *Heliyon* 9(6), article e17021. https://doi.org/10.1016/j.heliyon.2023.e17021

Hui, Y., Zhang, L., Zhang, J., *et al.* (2024). "Pickering emulsions stabilized by soy protein/proanthocyanidins nanocomplexes: Physicochemical properties and *in vitro* release properties. *Colloids and Surfaces A*. https://doi.org/10.1016/j.colsurfa.2024.134711

Jeyanthi, V., Velusamy, P., Kumar, G. V., and Kiruba, K., (2021). "Effect of naturally isolated hydroquinone in disturbing the cell membrane integrity of *Pseudomonas aeruginosa* MTCC 741 and *Staphylococcus aureus* MTCC 740," *Heliyon* 7(5), article e07021. https://doi.org/10.1016/j.heliyon.2021.e07021

Johnson, E. A., and Brekke, C. J. (1983). "Functional properties of acylated pea protein isolates," *J. Food Sci.* 48, 722-725. https://doi.org/10.1111/j.1365-2621.1983.tb14883.x

Laemmli, U. K. (1970). "Cleavage of structural proteins during the assembly of the head of bacteriophage T4," *Nature* 227, 680-685. https://doi.org/10.1038/227680a0

Lan, T., Wang, X., Dong, Y.B., *et al.* (2024). "Fabrication of soy protein nanoparticles based on metal-phenolic networks for stabilization of nano-emulsions delivery system," *Food Chemistry* 448, article 139164. https://doi.org/10.1016/j.foodchem.2024.139164

Li, Y., Li, J., Lu, Y., and Ma, Y. (2024). "ZnO nanomaterials target mitochondrial apoptosis and mitochondrial autophagy pathways in cancer cells," *Cell Biochem. Funct.* 42, article e3909. https://doi.org/10.22541/au.169288569.97094751/v1

Li, Y., Liao, C., and Tjong, S. C. (2020). "Recent advances in zinc oxide nanostructures with antimicrobial activities," *Int. J. Mol. Sci.* 21, article 8836. https://doi.org/10.3390/ijms21228836

Lianou, A., Panagou, E. Z., and Nychas, G. (2023). "Meat safety—I. Foodborne pathogens and other biological issues," in: *Lawrie's Meat Science*, Elsevier, pp. 549-590. https://doi.org/10.1016/b978-0-323-85408-5.00015-7

Mammari, N., Lamouroux, E., Boudier, A., and Duval, R. (2022). "Current knowledge on the oxidative-stress-mediated antimicrobial properties of metal-based nanoparticles," *Microorganisms* 10, article 437. https://doi.org/10.3390/microorganisms10020437

Mbeh, D.A., Javanbakht, T., Tabet, L., Merhi, Y., Maghni, K., Sacher, E., and Yahia, L. (2015). "Protein corona formation on magnetite nanoparticles: Effects of culture medium composition, and its consequences on superparamagnetic nanoparticle cytotoxicity," *J. Biomed. Nanotechnol.* 11(5), article 828 840. https://doi.org/10.1166/jbn.2015.2000

Modi, S. K., Gaur, S., Sengupta, M., and Singh, M. S. (2023). "Mechanistic insights into nanoparticle surface-bacterial membrane interactions in overcoming antibiotic resistance," *Front. Microbiol.* 14, article 1135579. https://doi.org/10.3389/fmicb.2023.1135579

Monopoli, M. P., Walczyk, D., Campbell, A., Elia, G., Lynch, I., Bombelli, F. B., and Dawson, K.A. (2011). "Physical-chemical aspects of protein corona: Relevance to in vitro and in vivo biological impacts of nanoparticles," *J. Am. Chem. Soc*. 133(8), 2525-2534. https://doi.org/10.1021/ja107583h

Mosmann, T. (1983). "Rapid colorimetric assay for cellular growth and survival: Application to proliferation and cytotoxicity assays," *J. Immunol. Methods* 65, 55-63. https://doi.org/10.1016/0022-1759(83)90303-4

Mourad, A. N., Elariny, E. Y., Shindia, A., El-Saber, M. M., Alsharif, A., Soliman, M. M., Gaber, A., Alotaibi, K. S., and Osman, A. J. (2025). "Green synthesis of selenium nanoparticles, and its conjugation with antibacterial proteins for enhancing their antibacterial activity," *Bioorg. Chem*. 108443. https://doi.org/10.1016/j.bioorg.2025.108443

Nanda, A., and Saravanan, M. (2009). "Biosynthesis of silver nanoparticles from *Staphylococcus aureus* and its antimicrobial activity against MRSA and MRSE," *Nanomedicine: Nanotechnology, Biology and Medicine* 5, 452-456. https://doi.org/10.1016/j.nano.2009.01.012

Osman, A. O., Mahgoub, S. A., and Sitohy, M. Z. (2013). "Preservative action of 11S (glycinin) and 7S (β-conglycinin) soy globulin on bovine raw milk stored either at 4 or 25 C," *J. Dairy Res*. 80, 174-183. https://doi.org/10.1017/s0022029913000095

Pujara, N., Jambhrunkar, S., Wong, K.Y., *et al.* (2017). "Enhanced colloidal stability, solubility and rapid dissolution of resveratrol by nanocomplexation with soy protein isolate," *Journal of Colloid and Interface Science* 448, 303-308. https://doi.org/10.1016/j.jcis.2016.11.015

Rashidi, M., Seghatoleslam, A., Namavari, M., Amiri, A., Fahmidehkar, M. A., Ramezani, A., Eftekhar, E., Hosseini, A., Erfani, N., and Fakher, S. (2017). "Selective cytotoxicity and apoptosis-induction of *Cyrtopodion scabrum* extract against digestive cancer cell lines," *Int. J. Cancer Manag*. 10(5), article e8633. https://doi.org/10.5812/ijcm.8633

Reddy, N., and Rapisarda, M. (2021). "Properties and applications of nanoparticles from plant proteins," *Materials* 14(13), article ma14133607. https://doi.org/10.3390/ma14133607

Safa, A., Shafiei, M., Sangari, A. N., Roudbordeh, A. N., Ghaderibarmi, F., Kohsarian, M., Mohaghegh, R., Maaf, Z. M., Valisaraei, M. E., and Faraji, Z. (2025). "Targeted anticancer effects of Juglone-ZnO nanoparticles *via* cell cycle arrest and caspase-mediated apoptosis in colon cancer cells," *Sci. Rep*. 16, article 1513. https://doi.org/10.1038/s41598-025-31183-y

Schmidt, M. (2023). "Nanoparticles incorporated soy protein isolate for emerging applications in medical and biomedical sectors," *Foods* 13(17), article 2812. https://doi.org/10.21741/9781644902172-11

Sitohy, M., Mahgoub, S., and Osman, A. (2011). "Controlling psychrotrophic bacteria in raw buffalo milk preserved at 4 C with esterified legume proteins," *LWT-Food Sci. Technol.* 44, 1697-1702. https://doi.org/10.1016/j.lwt.2011.03.008

Sitohy, M., and Osman, A. J. F. C. (2010). "Antimicrobial activity of native and esterified legume proteins against Gram-negative and Gram-positive bacteria," *Food Chem.* 120, 66-73. https://doi.org/10.1016/j.foodchem.2009.09.071

Taiwo, O. R., Onyeaka, H., Oladipo, E. K., Oloke, J. K., and Chukwugozie, D. C. (2024). "Advancements in predictive microbiology: Integrating new technologies for efficient food safety models," *Int. J. Microbiol.* 2024, article 6612162. https://doi.org/10.1155/2024/6612162

Tansaz, S., and Boccaccini, A.R. (2016). "Biomedical applications of soy protein: A brief overview," *Journal of Biomedical Materials Research Part A* 104(2), 553-569. https://doi.org/10.1002/jbm.a.35569

Tewatia, K., Sharma, A., and Kumar, A. (2022). "Synthesis of ZnO/rGO and green approach for its reduction by ascorbic acid," in: *AIP Conference Proceedings*, 070006. https://doi.org/10.1063/5.0118780

Turmagambetova, A. S., Sokolova, N. S., Bogoyavlenskiy, A. P., Berezin, V. E., Lila, M. A., Cheng, D. M., and Dushenkov, V. (2015). "New functionally-enhanced soy proteins as food ingredients with anti-viral activity," *Virusdisease*. 26, 123-132. https://doi.org/10.1007/s13337-015-0268-6

Vaara, M., and Vaara, T. (1981). "Outer membrane permeability barrier disruption by polymyxin in polymyxin-susceptible and-resistant Salmonella typhimurium," *Antimicrob. Agents Chemother.* 19, 578-583. https://doi.org/10.1128/aac.19.4.578

Wiegand, I., Hilpert, K., and Hancock, R. (2008). "Agar and broth dilution methods to determine the minimal inhibitory concentration (MIC) of antimicrobial substances," *Nat. Protoc*. 3, 163-175. https://doi.org/10.1038/nprot.2007.521

Wu, C., Wu, F., Ju, Q., Zhang, Y., Yuan, Y., Kang, S., Hu, Y., and Luan, G. (2023). "The role of β-subunit in emulsifying performance of β-conglycinin," *Food Hydrocoll.* 141, article 108694. https://doi.org/10.1016/j.foodhyd.2023.108694

Yang, Z., Li, D., Chen, L., Zhang, W., Jiang, L., Huang, Z., and Tian, T. (2025). "Structural characteristics, techno-functionalities, innovation applications and future prospects of soybean β-conglycinin/glycinin: A comprehensive review," *Crit. Rev. Food Sci. Nutr.* 65, 6410-6427. https://doi.org/10.1080/10408398.2024.2440601

Zhou, K., Zhou, W., Li, P., Liu, G., Zhang, J., and Dai, Y. (2008). "Mode of action of pentocin 31-1: An antilisteria bacteriocin produced by Lactobacillus pentosus from Chinese traditional ham," *Food Cont.* 19, 817-822. https://doi.org/10.1016/j.foodcont.2007.08.008

Article submitted: June 28, 2026; Peer review completed: July 19, 2026; Revised version received and accepted: August 11, 2026; Published: August 27, 2026.
DOI: 10.15376/biores.21.4.10127-10148